Journal of Sustainable Development of Smart Energy Networks
https://www.sdewes.org/jsdsen

Year 2026, Volume 1, Issue 1, 2030678

Original Research Article

Flexible Solid Oxide Fuel Cells for Low-Carbon Electricity: A Techno-Economic Assessment of Hydrogen from Biomethane and Bioethanol

Gustavo B. F. da Silva[*1], Stefano F. Interlenghi[1], Julliana M. Gonçalves[1], Jeiveison G. S. S. Maia[2], Alexandre M. Teixeira[3]*
[1]Instituto SENAI de Inovação em Biossintéticos e Fibras, Parque Tecnológico, Rio de Janeiro, Brasil
e-mail: GBFsilva@firjan.senai.br
[2]Universidade Federal do Rio de Janeiro, Cidade Universitária, Rio de Janeiro, Brasil
e-mail: jeiveison@peq.coppe.ufrj.br
[3]Repsol Sinopec Brasil, Rio de Janeiro, Brasil
e-mail: alexandre.mendonca@repsolsinopec.com

Cite as: da Silva, G., Interlenghi, S., Gonçalves, J., Maia, J., Teixeira, A., Flexible Solid Oxide Fuel Cells for Low-Carbon Electricity: A Techno-Economic Assessment of Hydrogen from Biomethane and Bioethanol, J. sustain. dev. smart. en. sys., 1(1), 2030678, 2026, DOI: https://doi.org/10.13044/j.sdsen.d3.0678

ABSTRACT

This paper presents a techno-economic evaluation of solid oxide fuel cells powered by hydrogen produced from hybrid systems using either ethanol or methane. Steady-state models were developed based on equations and parameters reported in the literature. By integrating simulation results with cost estimations, the study provides insights into the viability and competitiveness of cell-based systems for low-carbon energy generation. Scenarios involving 21 MW (biogas) and 101.91 GWh/year of electricity production were investigated. Results indicate that cell modules are the primary cost drivers, accounting for approximately 70–80% of total capital investment, while ethanol procurement emerged as the main contributor to operational expenditures in relevant scenarios. Comparative analysis showed that the systems can achieve lower levelized costs of electricity than conventional back-up technologies such as photovoltaic systems coupled to batteries and diesel generators—reaching $112.70/MWh and $166.93/MWh in the most favorable cases. These findings highlight the technological and economic potential and suggest that, with continued development and scale-up, such systems could become increasingly competitive in future energy markets.

KEYWORDS

SOFC, Hydrogen, Biomethane, Bioethanol, Energy Efficiency, Techno-economic Analysis, Process Simulation, Aspen.

INTRODUCTION

We believe that it would be very useful if the authors reviewed the manuscripts that have already been published in Journal of Sustainable Development of Energy, Water and Environment Systems. Such an effort would not only improve the quality of your manuscript but also promote the awareness of the available information resources that exist in the structure of Journal of Sustainable Development of Energy, Water and Environment Systems. Please use the online open access for the literature review: The growing demand for more efficient and sustainable energy sources is driving the development of advanced technologies for electricity generation. Among

[*] Corresponding author

these technologies, Solid Oxide Fuel Cells (SOFCs) stand out due to their high efficiency, fuel flexibility, and potential for both stationary and mobile applications [1]. Unlike other fuel cells, SOFCs operate at high temperatures (650 – 1000°C) [2], enabling internal fuel reforming and reducing operational costs by enhancing system self-sufficiency when coupled with a reforming process.

The integration of renewable fuels, such as ethanol, with conventional sources like methane opens new opportunities for hybrid power generation systems. Ethanol, derived from biomass, follows a closed carbon cycle, significantly reducing net CO_2 emissions, while methane, being widely available, ensures operational reliability. Further, if methane is from renewable origin (biomethane), it follows a closed carbon cycle as well. Therefore, developing hybrid fuel cells based on SOFC technology represents a promising strategy for enhancing energy efficiency and reducing environmental impacts of the electricity generation sector.

SOFCs operate through the electrochemical conversion of fuel into electricity, eliminating the need for direct combustion. They consist of three primary layers: an anode electrode, a solid electrolyte, and a cathode electrode. During operation, oxygen from the air is reduced at the cathode, forming oxygen ions (O^{2-}), which migrate through the electrolyte to the anode. At the anode, these ions react with fuel (such as hydrogen, methane, or ethanol), generating electricity, water vapor, and, depending on the fuel used, carbon dioxide [3].

Several studies have analysed the modelling and performance of SOFC units under different operating conditions [4]. Other works have investigated the influence of key design parameters on polarization behaviour and overall cell response [5]. Additional evaluations have also examined the thermodynamic performance of SOFC-based power systems, considering energy and exergy indicators [6]. Individually, these studies strengthen the understanding of SOFC behaviour from the cell level to the system scale. Additionally, economic evaluations of hybrid power generation systems integrating SOFCs with reforming processes have been conducted, comparing their feasibility and potential with existing energy sources [7, 8]. These studies provide insights into the economic viability of such systems, identifying key financial constraints and guiding future development strategies. However, limited research has been conducted on the evaluation of hybrid fuel cells utilizing fuel blends in reforming processes, particularly regarding their scalability, operational challenges, and financial implications.

This paper discusses the use of SOFCs for power generation based on a combination of (bio)ethanol and (bio)methane as fuels. It analyses thermodynamic aspects, the implementation of electrochemical reaction modelling in the system, and its behaviour under different configurations, operational factors, and technological challenges associated with this type of system. The study also considers the advantages and limitations of each fuel and explores potential strategies for performance optimization. Furthermore, beyond system modelling, this work presents an economic analysis of low-carbon electricity production and compares it with other off-grid energy sources.

METHODS

The methodology developed in this work encompasses the study and implementation of process simulations in Aspen Plus version 14 software to obtain mass and energy balances. Different scenarios were evaluated, considering both biogas and ethanol-based systems. Additional scenarios were developed to compare the use of natural gas from the grid with biogas derived from the anaerobic digestion of biomass feedstock. The processing capacity considered was 21 MW of electricity, equivalent to 431.04 kmol/h of biogas [9]. Current process simulators do not have an implemented block to represent the SOFC. Thus, a self-developed model of the SOFC was developed and implemented in the simulator. Upon completing each scenario and obtaining the corresponding technical coefficients, equipment was sized, and cost estimates were generated using Aspen Process Economic Analysis (APEA). Finally, an economic assessment was conducted based on the principles of engineering economics [10], evaluating the accumulated cash flow over the required investment horizon. Key economic indicators were extracted, and a comparative analysis was performed with off-grid energy sources to assess the potential for electricity generation using commercially established technologies.

Process flow diagram

The complete process for the base case of the integrated system developed in Aspen Plus is presented in Figure 1. In summary, the system is divided into three sections: the first corresponds to the sulphur removal zone from biogas, the second to CO_2 removal, and the third to the reforming-SOFC zone. Simulation assumptions were extracted from specific literature and can be found in Table 1. In the first zone, the biogas stream is fed into a scrubber, where a sodium hydroxide solution is pumped in counter current. In this process, the gaseous H_2S in the stream reacts with NaOH to form NaHS. The treated gas stream, now with low contents of H_2S, exits at the top and continues through the process, while the bottom stream is sent to a bioreactor. In this aerated bioreactor, NaHS is converted into Na_2SO_4 and elemental sulphur. The mixture is then sent to a settler for the removal of solid particles, and the liquid phase is recycled back to the scrubber, reducing sodium hydroxide solution feed. This process, known as THIOPAQ, is widely used on an industrial scale [11]. In the simulation environment, stoichiometric reactors (RStoic) were used, with predefined conversion parameters seen in Table 1. The non-random two liquid (NRTL) and PR-BM are adopted for properties estimation in the unit models [12].

In the CO_2 removal section, the CO_2-rich stream is pressurized and fed into a washing tower, where it flows counter currently with water. The treated biomethane stream exits at the top and is directed to the reforming unit, while the effluent stream is sent to a flash vessel and subsequently to a stripping tank. In this tank, a heated steam stream is introduced to desorb the residual CO_2 from the liquid phase, which is then recirculated within the process.

In the reforming-SOFC unit, ethanol, water, and biomethane streams are preheated before being fed into the reformer. Several scenarios were evaluated, including different ethanol-to-methane compositions, as well as cases using either natural gas from the grid or biomethane. The reformer outlet stream, which is rich in hydrogen, is then directed to the SOFC module, which supplies electrical energy to the plant. After passing through the SOFC, the residual gas stream is sent to a combustion reactor, which provides heat for the plant's energy integration. In this system, the reformer was simulated using a tubular reactor (RPlug) with implemented kinetic reactions. The SOFC module was modelled by simulating the anode and cathode separately: the anode as an equilibrium reactor (RGibbs) and the cathode as a separator block (Sep) capable of enriching the stream with O_2 before being fed into the anode.

Heterogeneous Kinetic Reactor

Hydrogen is a key element in the transition to a low-emission and energy-efficient economy. Among various production methods, steam reforming (SR) is the most widely used due to its high efficiency and hydrogen yield. Ethanol, derived from renewable biomass, has emerged as a promising feedstock for ethanol steam reforming (ESR) [22]. The ESR process is endothermic and constrained primarily by equilibrium rather than reaction kinetics, making in-situ hydrogen separation a potential optimization strategy [29].

ESR involves multiple competing reactions, including ethanol steam reforming, the water-gas shift reaction (WGSR), ethanol decomposition (ED), and steam methane reforming (SMR), represented in equations (1) to (4). Both ESR and SMR require high temperatures for effective hydrogen production. The process generates H_2, CO, CO_2, and CH_4, with kinetics playing an important role in the reformer operation [30, 31]. These kinetics fall into two categories: general reforming reactions (SMR and WGSR) and ethanol-specific reactions (ESR and ED). Heterogeneous Kinetic Reactor

Table 1. Main premises and bases for simulation.

Parameters	Units	Value	Source
Biogas composition			
Methane	[%]	50	[13]
CO_2	[%]	45	[13]
H_2O	[%]	4.8	[13]
H_2S	[ppm]	2,800	[13]
Natural gas composition			
Methane	[%]	~93	[14]
$N_2 + CO_2 + O_2$	[%]	~7	[14]
H_2O	[%]	~0,3	[14]
H_2S	[ppm]	<10	[14]
H_2S removal section			
Temperature	[°C]	25	[15]
Pressure	[bar]	1.2	[15]
H_2S to NAHS conversion	[%]	99.8	[15]
NAHS to S conversion	[%]	96.5	[15]
NaHS to Na_2SO_4 conversion	[%]	3.5	[15]
Air to biogas ratio	[mol/mol]	stoichiometric	[16]
NaOH:S mass ratio	[%]	44	[16]
CO_2 removal section			
Scrubber pressure	[bar]	8	[17]
Scrubber number of stages	–	15	[17]
Stripper pressure	[bar]	1	[17]
Stripper number of stages	–	5	[17]
Air to biogas molar ratio	[mol/mol]	2:1	[17]
Methane recovery	[%]	>97	[18]
CO_2 removal efficiency	[%]	>90	[18]
SOFC-Reformer			
Reformer pressure	[bar]	1.2	[19]
Reformer inlet temperature	[K]	650	[20, 21]
Reformer temperature	[K]	923	[22, 23]
SOFC Temperature	[*K*]	1,273	[24. 25]
Fuel utilization factor	[%]	0.85	[26, 27]
Air utilization factor	[%]	0.19	[28]
Inverter efficiency	[%]	0.92	[28]
Cell area	[m]	0.045	–
Number of stacks per cells	–	350	–
Number of modules	–	48	–
Cells' desired power	[W/cell]	0.125	–

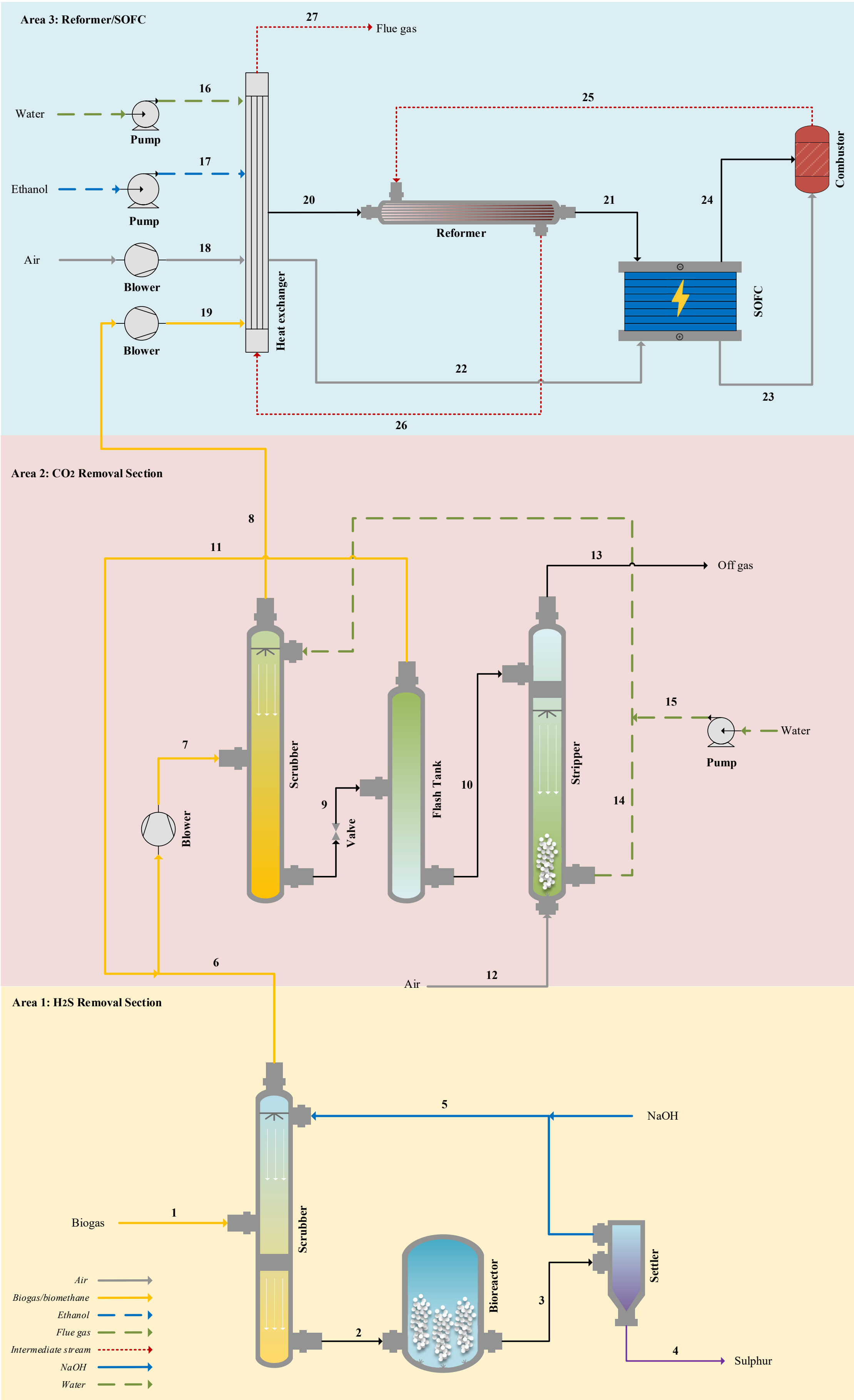
Area 3: Reformer/SOFC
27
Flue gas
16
Water
Pump
17
Ethanol
Pump
18
Air
Blower
19
Blower
Heat exchanger
20
25
Reformer
21
24
Combustor
SOFC
22
23
26
Area 2: CO2 Removal Section
8
11
13
Off gas
15
Water
Pump
7
Scrubber
Flash Tank
Stripper
9
Valve
10
14
Blower
6
Air
12
Area 1: H2S Removal Section
5
NaOH
Biogas
1
Scrubber
Bioreactor
Settler
2
3
4
Sulphur
Air
Biogas/biomethane
Ethanol
Flue gas
Intermediate stream
NaOH
Water

Figure 1. Process flow diagram of the integrated process.

$$C_2H_5OH + H_2O \rightleftarrows 2CO + 4H_2 \tag{1}$$

$$CO + H_2O \rightleftarrows CO_2 + H_2 \tag{2}$$

$$C_2H_5OH \rightleftarrows CO + H_2 + CH_4 \tag{3}$$

$$CH_4 + H_2O \rightleftarrows CO + 3H_2 \tag{4}$$

A key challenge in steam reforming is coke formation, which deactivates catalysts over time. Since this phenomenon is highly catalyst-specific and difficult to model, it has been excluded in this study to simplify the modelling approach. As a result, the simulated outcomes may be optimistic, with actual performance depending on catalyst behaviour. In this project, the kinetic model was implemented in a simulation environment using Aspen Plus, specifically in a plug flow reactor (RPlug). The system was divided into two reaction sets due to its hybrid nature. The first set primarily corresponds to methane reforming reactions, whose kinetics are well-studied and extensively documented in the literature. The second set is related to ethanol reactions, which exhibit specific characteristics due to their more complex molecular structure and the influence of intermediate products. This approach enables a more accurate modelling process by accounting for the differences in reaction mechanisms and kinetic limitations of each fuel. For the WGSR, the reaction kinetics follow the Langmuir-Hinshelwood-Hougen-Watson (LHHW) model based on literature [32], and its corresponding parameters can be found at Table 2. The reaction rate expressions are as follows:

$$r_{SMR} = \frac{k_{SMR}}{{P_{H_2}}^{2,5}}\left(P_{CH_4}P_{H_2O} - \frac{{P_{H_2}}^3 P_{CO}}{K_{SMR}}\right)(DEN)^{-2} \tag{5}$$

$$r_{WGS} = \frac{k_{WGS}}{P_{H_2}}\left(P_{CO}P_{H_2O} - \frac{P_{H_2}P_{CO_2}}{K_{WGS}}\right)(DEN)^{-2} \tag{6}$$

$$DEN = 1 + K_{CO}P_{CO} + K_{H_2}P_{H_2} + K_{CH_4}P_{CH_4} + \frac{K_{H_2O}P_{H_2O}}{P_{H_2}} \tag{7}$$

Where and, r_{SMR} and r_{WGS} denote the reaction rates of SMR and WGS, respectively. P_{H_2}, P_{CH_4}, P_{H_2O}, P_{CO} and P_{CO_2} represent the partial pressures of hydrogen, methane, water, carbon monoxide, and carbon dioxide in bar, respectively. k_{SMR} and K_{WGS} are chemical equilibrium constants of SRM and WGS; and K_{CO}, K_{H2}, K_{CH4}, and K_{H2O} are the adsorption constants for carbon monoxide, hydrogen, methane, and water.

Table 2. Kinetics parameters to SMR and WGSR reactions.

Parameters	Units	Value
SMR Pre-exponential factor	[$\mathrm{kmol \cdot Pa^{0.5} \cdot kg_{cat}^{-1} \cdot h^{-1}}$]	7.592E+16
WGSR Pre-exponential factor	[$\mathrm{kmol \cdot Pa^{-1} \cdot kg_{cat}^{-1} \cdot h^{-1}}$]	5.707E+08
SMR Activation energy	[kJ/mol]	292.922
WGSR Activation energy	[kJ/mol]	114.121

The equilibrium constants K_{SMR} and K_{WGS} can be found in literature and are typically either constant or temperature dependent. In this work, these constants are calculated based on the equations from Rahimpour *et al*. [33]:

$$K_{SMR} = exp\left(30.144 - \frac{26{,}830}{T}\right) \tag{8}$$

$$K_{WGS} = exp\left(-4.036 + \frac{4{,}400}{T}\right) \tag{9}$$

To accurately model ethanol reforming, the selected reaction set was designed to capture not only the primary reaction pathways but also the formation of by-products and intermediates that significantly influence process behaviour. By distinguishing the kinetics of ethanol from those of methane, the model was tailored to account for the specific characteristics of thermal decomposition and the interactions between reactants and the catalyst — both fundamental for hydrogen production [23]. The inclusion of key reactions such as ethanol dehydrogenation (EH, eq.(10), direct ethanol decomposition (ED eq. ((11)), and acetaldehyde reforming (AR eq.(12)) enables better control over intermediates like carbon monoxide (CO), methane (CH_4), and acetaldehyde (CH_3CHO). Although the WGSR reaction is incorporated in the model, it was deactivated in the simulation environment to prevent redundancy and interference with other implemented models.

$$C_2H_5OH \rightarrow CH_3CHO + H_2 \tag{10}$$

$$C_2H_5OH \rightarrow CO + H_2 + CH_4 \tag{11}$$

$$CH_3CHO + 2H_2O \rightarrow 2CO_2 + 5H_2 \tag{12}$$

These reactions were formulated based on the law of mass action and treated as direct functions of the reactant concentrations, suitable for gas-phase systems like this one. Applying the modified Arrhenius equation to the kinetic constants allows the model to consider temperature variations accurately, as the reaction rates are highly sensitive to thermal changes. All the parameters used are shown in Table 3 and the rates follow as:

$$r_{EH} = k_1 P_{C_2H_5OH} \tag{13}$$

$$r_{ED} = k_2 P_{C_2H_5OH} \tag{14}$$

$$r_{AR} = k_3 P_{CH_3CHO} P_{H_2O}^3 \tag{15}$$

$$k_j = k_{\infty j}\, exp\left(-E_{aj}\left(\frac{1}{RT} - \frac{1}{RT_{ref}}\right)\right) \tag{16}$$

Here, $k_\infty j$ is the pre-exponential factor, k_j the kinetic constant for each reaction, E_{aj} the activation energy, T the system temperature, T_{ref} the reference temperature, and $P_{\mathrm{C_2H_5OH}}$, P_{CO}, P_{H_2O}, $P_{\mathrm{CH_3}CHO}$ refer to the partial pressures of each component in bar.

Table 3. Kinetics parameters EH, ED and AR reactions

Parameters	Units	Value
EH Pre-exponential factor	[Mol/m³.min.bar]	2.10E+04
ED Pre-exponential factor	[Mol/m³.min.bar]	2.00E+03
AR Pre-exponential factor	[Mol/m³.min.bar⁴]	2.00E+05
EH Activation energy	[kJ/mol]	70
ED Activation energy	[kJ/mol]	130
AR Activation energy	[kJ/mol]	98

Reference temperature	[K]	793

Solid Oxide Fuel Cells Modelling

For the development of reaction modelling within the SOFC, it was necessary to implement phenomenological models that encompass the half-reaction of hydrogen combustion. Although it is well known that reforming reactions occur at high temperatures, it is common practice to assume that only hydrogen reacts in the medium to simplify the analysis.

For computational simulation, an equilibrium reactor (RGibbs) was implemented, where only the global reaction (19) was considered. The cathode reaction corresponds to the reduction of oxygen to form the ionic species (17). Hydrogen is adsorbed at the anode, while the oxide ion crosses the electrode and reacts with hydrogen at the anode-electrode interface (18), ultimately leading to global reaction (19). These steps are represented in equations (17) to (19).

$$0.5O_2 + 2e^- \rightarrow O^{2-} \tag{17}$$

$$H_2 + O^{2-} \rightarrow H_2O + 2e^- \tag{18}$$

$$H_2 + 0.5O_2 \rightarrow H_2O \tag{19}$$

For this study, a steady-state model was developed within a computational module to analyse and assess the system's performance, considering different input conditions. To achieve this, the cell operational potential must be defined, accounting for the electrochemical, thermodynamic, and transport phenomena that govern the system's behaviour, V_{Cell} (eq. ((20)) which is determined by the difference between the open-circuit electrochemical potential (V_{Nernst}, eq. ((21) and eq. ((22)) and the losses due to polarizations (V_{loss}, eq. ((23)). The Nernst equation calculates V_{Nernst} , considering the Gibbs free energy and the partial pressures of the reactant gases [9]. However, the actual cell potential is reduced by polarization losses, categorized as ohmic (V_{Ohm}), activation (V_{act}), and concentration (V_{Conc}). These losses stem from resistance to ion and electron flow, energy barriers at the electrodes, and mass transport limitations, respectively. Understanding these losses enables optimizing system efficiency by minimizing them to enhance net power output. All the parameters required for the modelling can be found in

Table 4.

This model, based on literature equations, provides a framework for predicting SOFC performance and optimizing its operation to maximize efficiency and power output.

$$V_{Cell} = V_{Nernst} - V_{loss} \tag{20}$$

$$V_{Nernst} = E^0 + \frac{RT_{SOFC}}{nF} ln\left(\frac{P_{H_2}P_{O_2}^{0,5}}{P_{H_2O}}\right) \tag{21}$$

$$E^0 = 1.253 - 2.4516 \cdot 10^{-4}\, T \tag{22}$$

$$V_{loss} = V_{Ohm} + V_{act} + V_{Conc} \tag{23}$$

In these equations, E^0 represents the standard potential of the cell at a reference temperature, T_{SOFC} is the system temperature in Kelvin, R is the gas constant (8.314 J/(mol·K)), n is the number of electrons transferred in the electrochemical reaction (for an SOFC, n = 2), F is Faraday's constant (96,485 C/mol), and P_{H_2}, P_{H_2O}, and P_{O_2} represent the partial pressures of hydrogen, water vapor, and oxygen gases, respectively.

Additionally, determining the cell's power output requires consideration of several factors, including the cell area, the fuel utilization factor, and the molar flow rate of hydrogen in the feed stream. The cell power (W) and the current density (i) can be expressed as:

$$V_{Cell} = V_{Nernst} - V_{loss} \tag{24}$$

$$W = iANV\eta_{inv} \tag{25}$$

$$i = \frac{2\mathrm{Fn}_{\mathrm{H_2cons}}}{NA} \tag{26}$$

Where i is the current density, A is the cell area, N is the number of cells, V is the cell voltage, η_{inv} is the inverter efficiency, and $\mathrm{n}_{\mathrm{H_2cons}}$, is the molar flow rate of hydrogen consumed. The fuel utilization factor (U_f) is defined in equation (27) as the ratio of the consumed hydrogen ($n_{H_{2,cons}}$) to the available hydrogen in the feed $n_{H_{2,in}}$.

$$U_f = \frac{n_{H_{2,cons}}}{n_{H_{2,in}}} \tag{27}$$

In this model, maximizing power output requires optimizing each of these variables, as they directly impact the efficiency and overall performance of the fuel cell system. To accurately account for polarization losses, the equations were categorized into three distinct types: ohmic, activation, and concentration polarizations. Each of these losses originates from different physical and electrochemical phenomena, influencing the system's voltage drop and energy conversion efficiency. For the ohmic, it follows as:

$$V_{Ohm} = \mathrm{i}\sum\nolimits_k r_k \tag{28}$$

$$r_k = \frac{\rho_{\mathrm{k}}\delta_k}{A} \tag{29}$$

$$\rho_k = A_K exp\left(\frac{B_K}{T_{SOFC}}\right) \tag{30}$$

Where r_k represents the resistances associated with the anode, cathode, electrolyte, and interconnections; ρ_{k} is the specific resistivity of each material; δ_k is the material thickness; and A is the cell exchange area. A_K and B_K are empirical factors, and T_{SOFC} is the system temperature.

Activation polarization arises from electrochemical reactions and can be described by the following Butler-Volmer equation:

$$i = i_0\left[\exp\left(\frac{\beta n_e F V_{act}}{RT}\right) - \exp\left(-\frac{(1-\beta)n_e F V_{act}}{RT}\right)\right] \tag{31}$$

Where β is the transfer coefficient and i_0 is the exchange current density. Theoretically, it represents the fraction of the activation polarization that influences the energy barriers of the electrochemical reaction. In fuel cell applications, a typical value for β is 0.5 [6]. The previous equation then can be simplified by:

$$V_{act} = \frac{2RT}{n_e F} sinh^{-1}\left(\frac{i}{2i_o}\right) \tag{32}$$

The current exchange densities for the anode and cathode are as follows:

$$i_0^{an} = \gamma^{an}\left(\frac{\mathrm{p_{H_2}}}{\mathrm{P}}\right)\left(\frac{\mathrm{P_{H_2O}}}{\mathrm{P}}\right)\exp\left(-\frac{\mathrm{E^{an}}}{\mathrm{RT}}\right) \tag{33}$$

$$i_0^{ca} = \gamma^{an}\left(\frac{\mathrm{p_{O_2}}}{\mathrm{P}}\right)^{0,25} \exp\left(-\frac{\mathrm{E^{ca}}}{\mathrm{RT}}\right) \tag{34}$$

Where γ is the pre-exponential factor, P is the system pressure, p_i is the partial pressure of each component, and E is the activation energy.

Concentration polarization occurs when the input is consumed at the electrode surface faster than it can be supplied by diffusion, creating a concentration gradient. The total concentration polarization V_{conc} in SOFC is given by the equation (35) below:

$$V_{conc} = V_{conc}^{an} + V_{conc}^{ca} \tag{35}$$

$$V_{conc}^{an} = \frac{RT}{n_e F}\ln\left(\frac{1-\frac{i}{i_{L,H_2}}}{1+\frac{i}{i_{L,H_2O}}}\right) \tag{36}$$

$$V_{conc}^{ca} = \frac{RT}{n_e F}\ln\left(\frac{1}{1-\frac{i}{i_{L,O_2}}}\right) \tag{37}$$

Where V_{conc}^{an} and V_{conc}^{ca} represent concentration polarizations at the anode and cathode, respectively. i_{L,H_2} i_{L,H_2O}, i_{L,O_2}represent the limiting current densities for hydrogen, water vapor, and oxygen, respectively.

To calculate the limiting current density, it is necessary to determine both the Knudsen diffusivity and the binary diffusivity. Some of these diffusivities are obtained through empirical models based on particle collision parameters, which influence mass transport within the system. For this study, these parameters were derived from values reported in the literature [12, 14] based on Leonnard-Jones potential [31], ensuring consistency with established experimental and theoretical data. To calculate the effective diffusivity of hydrogen in a porous medium the equation follows as:

$$\frac{1}{D_{eff,H_2}} = \frac{\varepsilon}{\tau}\left(\frac{1}{D_{i,k}} + \frac{1}{D_{i,j}}\right) \tag{38}$$

Where D_{eff,H_2}, is the effective diffusivity of hydrogen, ε is the electrode porosity, and τ is the tortuosity factor. Here, $D_{i,k}$ is the Knudsen diffusivity and $D_{i,j}$ is the binary diffusivity. The equations for calculating Knudsen diffusivity $D_{i,k}$ and binary diffusivity $D_{i,j}$ are:

$$D_{i,k} = \frac{2}{3} r_{por}\sqrt{\frac{8RT}{\pi M_i}} \tag{39}$$

$$D_{i,j} = \frac{0.0018583\left(\frac{1}{M_i}+\frac{1}{M_j}\right)^{0.5} T^{\frac{3}{2}}}{P\Omega_{Di,j}\sigma_{i,j}^2} \tag{40}$$

Where r_{por} is the pore radius, M_i and M_j are the molar masses of species i and j, $\Omega_{Di,j}$ is the collision integral, and $\sigma_{i,j}^2$ is the collision diameter, a parameter that reflects the "width" of the molecules and affects collision frequency.

Table 4. Main premises and base for the SOFC modelling

Parameters	Units	Value	Source
Ohmic losses			
Anode empirical factor A_K	[Ω.m]	2.98E-05	[4]
Anode empirical factor B_K	[K]	-1.39E+03	[4]
Anode thickness	[m]	1.00E-04	[4]
Cathode empirical factor A_K	[Ω.m]	8.11E-05	[4]
Cathode empirical factor B_K	[K]	6.00E+02	[4]
Cathode thickness	[m]	2.20E-03	[4]
Electrolyte empirical factor A_K	[Ω.m]	2.94E-05	[4]
Electrolyte empirical factor B_K	[K]	1.04E+04	[4]
Electrolyte thickness	[m]	4.00E-05	[4]
Interconnection empirical factor A_K	[Ω.m]	1.20E-03	[4]
Interconnection empirical factor B_K	[K]	4.69E+03	[4]
Interconnection thickness	[m]	8.50E-05	[4]
Activation polarization			
Anode pre-exponential factor	[A/m²]	2.13E+08	[5, 6]
Cathode pre-exponential factor	[A/m²]	1.49E+10	[5, 6]
Anode activation energy	[J/mol]	1.00E+05	[5, 6]
Cathode activation energy	[J/mol]	1.60E+05	[5, 6]
Concentration polarization			
Pours radium	[m]	5.00E-05	[24]
Porosity	–	0.3	[24]
Tortuosity	–	6	[24]

Multiple Cases Specifications

For the process configuration, multiple scenarios were implemented to investigate the impact of the methane-to-ethanol ratio on operational feasibility. Five distinct scenarios were evaluated for biogas, varying the ethanol-biomethane ratio in the reformer feed. The analysed proportions were 0% biogas (100% ethanol), 25% biogas (75% ethanol), 50% biogas (50% ethanol), 75% biogas (25% ethanol), and 100% biogas (0% ethanol). The feed stream dilution was adjusted so that the ethanol flow rate served as the reference parameter. The molar water-to-carbon ratio was maintained at 3:1 across all scenarios. The chosen baseline case was 50% biogas:50% ethanol, in which the hydrogen flow rate at the reformer outlet was 9,000 Nm³/h. For the remaining scenarios, the feed flow rate was adjusted to ensure that hydrogen production remained constant. This adjustment was performed in the simulation environment by a design spec, ensuring the expected values converged. Five natural gas scenarios were also tested replacing biogas stream feed. For these scenarios, the same adjustment strategies were applied. Since natural gas is acquired with the compositional specifications needed, the biogas pre-treatment area was omitted. Table 5 presents the flow rate specifications for each scenario, considering ethanol, biogas, and natural gas streams. To emphasize, all scenarios were simulated using the same molecule (methane). In the scenario involving biogas, pre-treatment units must be acquired, whereas in the natural gas scenarios, the gas is already purchased with ideal technical specifications.

Table 5. Specification of each case implemented in the project

Parameters	Tag name	Biogas feed (kg/h)	Ethanol feed (kg/h)	Natural gas feed (kg/h)
Case 1	100% Biogas	7,589	–	–
Case 2	75% Biogas	5,589	1,738	–
Case 3	50% Biogas	3,520	3,376	–
Case 4	25% Biogas	1,789	4,561	–
Case 5	0% Biogas	–	5,964	–
Case 6	100% Natural Gas	–	–	2,280
Case 7	75% Natural Gas	–	1,738	1,679
Case 8	50% Natural Gas	–	3,376	1,066
Case 9	25% Natural Gas	–	4,561	538
Case 10	0% Natural Gas	–	5,964	–

Economic Assessment

The economic assessment was conducted in several stages. Initially, after the mass and energy balance estimation based on Aspen Plus results, the equipment was sized and quoted using the APEA methodology. Costs were estimated not only for the equipment but also for the overall infrastructure, including installation, freight, piping, electrification, administrative expenses, land acquisition, project contingency, and other associated costs, thereby consolidating the capital expenditures (CAPEX). Based on calculated CAPEX, the total investment costs (TIC) were estimated by incorporating working capital and start-up costs. Subsequently, following the principles of economic engineering outlined by Turton [10], operational expenditure (OPEX) was estimated, divided into variable costs—associated with raw materials—as well as direct and indirect field costs and additional expenses. These costs also include auxiliary process expenses necessary for system maintenance and operation, such as administrative costs, research and development, payroll for workers, product distribution and selling, among others. Finally, a cumulative and discounted cash flow was constructed, linked to a minimum attractiveness rate of return (MARR), allowing for the evaluation of key economic indicators, such as net present value (NPV), payback time, and electricity minimum selling price ($/MW). Additionally, the Levelized Cost of Electricity (LCOE, $/MW) was used to compare electricity production via SOFC with other typical back-up systems, such as conventional fuel cells, solar energy coupled with batteries, and diesel engines. Appendix A of this work presents typical ranges for OPEX composition, with median values adopted for calculations. Furthermore, Table 5 and Table 6 provide the prices of the raw materials used and the assumptions considered in calculating the electricity selling price.

Table 6. Prices for raw material and utilities

Parameters	Units	Value	Source
Raw material			
Biogas	[USD/m³]	0.07	[35,36]
Natural Gas	[USD/m³]	0.16	[37]
Ethanol	[USD/t]	572.7	[38]
Chemical inputs			
NaOH	[USD/t]	14.58	[38]
Process water	[USD/t]	0.05	[38]
Byproducts and credits			
Sulphur	[USD/t]	900	[38]

Table 7. Main premises and bases to calculate the minimum price of electricity

Parameters	Units	Value
Investment Horizon	[years]	10
Land Cost	[millions of dollars]	1.0% of CAPEX
Engineering, Procurement, and Production Time	[years]	1
Financing Type	–	None
MARR	[%]	14.55
Corporate Tax Rate	[%]	34
Depreciation Method	–	Linear
Depreciation Period	[years]	10

RESULTS AND DISCUSSION

To assess the behaviour of ohmic polarization through changes in temperature and current density, an experiment was conducted based on the SOFC cell modeling presented in the previous section. All parameters were held constant while the system temperature was varied. As shown in Figure 2(a), as temperature increases, ohmic polarization decreases. This trend is expected since higher temperatures reduce material resistivity, lowering the resistance term, therefore, polarization tends to decrease at the same current density. The results also show that higher current densities lead to greater polarization effects, which aligns with the understanding that polarization depends on both resistance and current density. Increasing current density with constant resistance raises ohmic polarization. Additionally, at lower temperatures, this effect is more pronounced as higher temperatures increase electron flow by lowering material resistance. Therefore, combining higher temperatures with lower current densities can help mitigate polarization effects.

To analyze the activation polarization behaviour, Figure 2(b), the same series of experiments was conducted. Results show that activation polarization is significantly lower at lower temperatures (973 K – 1073 K). This occurs because electrochemical reactions become more efficient as temperature rises. Higher temperatures reduce the energy activation required leading to a faster reaction rate and a lower overpotential needed to sustain a given current density. It also shows that activation polarization increases exponentially with current density, which is directly connected to voltage through the Butler-Volmer equation. Higher current densities demand an elevated reaction rate, thus requiring greater overpotential to overcome the activation energy barrier.

To validate the behavior of concentration polarization as a function of temperature and current density, new experiments were performed, and the results are shown in Figure 2(c). The data reveal that polarization increases exponentially as the current density approaches a certain limit. This is due to the increase in the rate of reactant consumption—oxygen at the cathode and fuel at the anode—on the electrode surfaces. To sustain this, reactant transport to the reaction sites must be sufficiently fast. However, oxygen transport to the cathode is limited by diffusion through the porous electrode layer and the interface conditions. As current density increases, an imbalance develops between oxygen consumption and supply, leading to a drop in local oxygen concentration. When the cell nears the limiting current density, where oxygen consumption equals its maximum transport rate, concentration polarization intensifies, and the potential increases nonlinearly. The cell voltage then shows asymptotic behavior, tending toward zero, as small increases in current density cause significant voltage drops. This defines the cell's practical limit, as oxygen is no longer available in sufficient quantities to sustain further reaction. Temperature also affects the limiting current density: at higher temperatures, oxygen diffusivity improves, enabling higher current densities before transport limitations occur. Thus, temperature plays an essential role in system performance by enhancing oxygen transport.

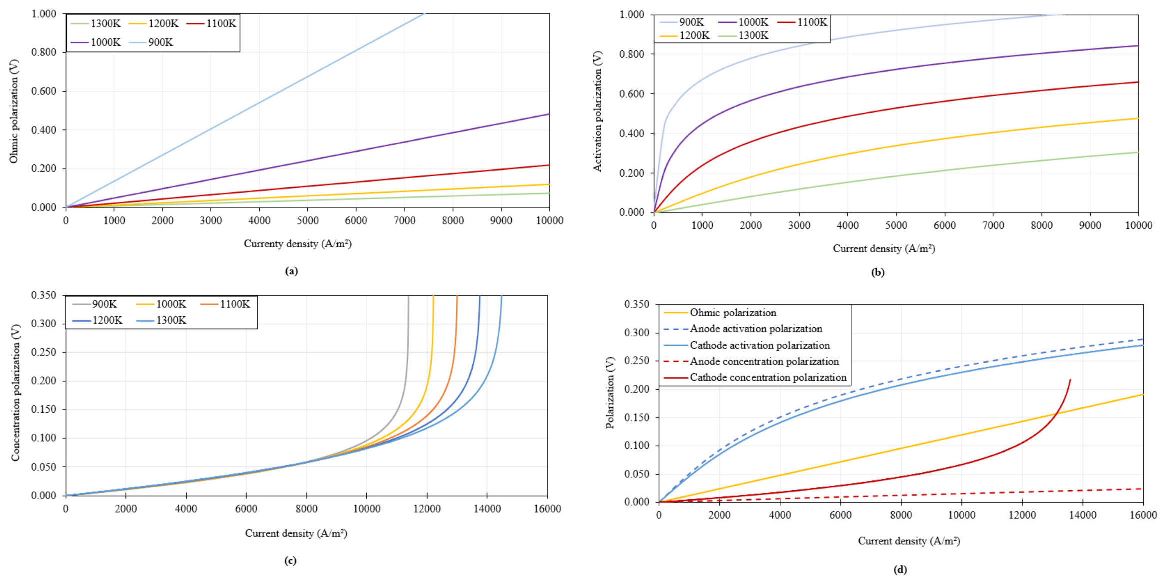

Figure 2. Polarization analysis as a function of current density at different temperatures: (a) Ohmic polarization; (b) Activation polarization; (c) Concentration polarization; (d) Comparison among the different polarization types.

In this comparative framework, Figure 2(d), it is observed that activation polarization, both at the anode and cathode, is the dominant form of polarization, with the anode polarization being more significant. This predominance is due to the higher activation energy required for the electrochemical reactions on the anode side, where fuel oxidation occurs, demanding more energy to overcome reaction barriers. Ohmic polarization ranks as the second most impactful factor, stemming primarily from the ionic resistance of the electrolyte and the electronic resistances of cell components. This resistance becomes more pronounced as current density increases, further affecting the overall performance. Concentration polarization has a minimal influence on low current densities, where diffusion limitations are less critical, and as a result, this polarization type is often neglected in literature. However, as current density approaches the limiting current density of the cathode, concentration polarization becomes more significant, potentially leading to rapid performance declines. To mitigate these effects, operating at lower current densities is recommended to avoid the increased influence of concentration polarization and to maintain stable cell performance. This general behaviour aligns well with established literature, supporting the validity of the proposed model across the various analyses performed in this study [4–6].

Figure 3 shows that for the same current density, power increases, which is associated with reduced polarization losses. For instance, at a current density of 3500 A/m², the voltages obtained are 0.276 V, 0.557 V, and 0.905 V at temperatures of 1000 K, 1100 K, and 1300 K, respectively. It also indicates the presence of an optimal for each of the systems studied. At this paper, it was focused on a temperature of 1,273 K (close to 1,300 K), where the maximum occurs near 12,000 A/m², which is very close to the oxygen limiting current density. The analysis shows that the cell voltage tends to decrease as the current density increases. This phenomenon occurs because polarizations increase with current density, leading to higher potential losses, which reduces the cell power until it reaches zero—this occurs when the current reaches the oxygen limiting current density. The results demonstrate a clear relationship between temperature, current density, and the resulting voltage and power output. Higher temperatures generally lead to increased power at a given current density, highlighting the importance of minimizing polarization losses to optimize performance. Furthermore, the identification of an optimal operating point underscores the need to carefully manage current density to avoid limitations, ensuring the effective operation of the system.

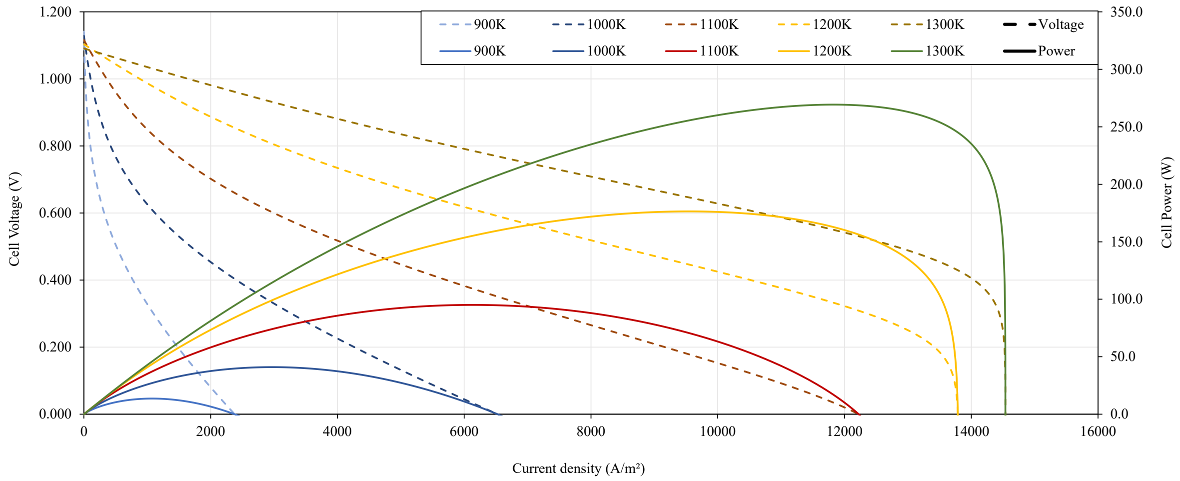

Figure 3. Cell voltage and cell power as a function of current density at different temperatures.

Investment costs

A portion of the equipment acquisition costs were estimated using APEA methodology, as previously described in this work, while specific CAPEX was applied to components, most notably the SOFC module — due to the limited information available in databases due to its technological maturity. SOFCs, being relatively new and still evolving, exhibit considerable variability in cost estimates, making them one of the main sources of uncertainty in the overall project assessment. The cost of SOFC systems generally depends on the power output, and for the purposes of this study, a specific cost of $2,000/kWh was adopted, based on literature data [39]. Given the high level of uncertainty associated with this parameter, a sensitivity analysis was conducted in subsequent sections to evaluate the impact of cost variations on the final electricity generation cost.

Table 8 summarizes the breakdown of cost for two scenarios: one based on biogas and the other on natural gas. In both cases, the SOFC unit represents the highest share of total plant costs, ranging between 60% and 70%. This proportion is consistent with figures reported in recent studies for this technology [40], reinforcing the validity of the adopted estimates.

For the remaining process units, cost estimates were derived from external validated sources. The steam reformer, for instance, was assigned a specific capital cost of approximately $237/kWh. The H_2S treatment and removal unit had an estimated installed cost of MM$3.347 for the base case, representing an 11% deviation from values reported in the literature [41]. This estimate was calculated using a scaling factor of 0.6 and included a monetary adjustment to align with the reported cost of $1,099.33/(Nm³/h).

Regarding the CO_2 removal system, the installed cost for the base case was estimated at MM$5.717, showing a deviation of about 12% from literature values [42,43]. According to the references, the typical cost for this technology is around £2,000/(Nm³/h), which, when converted and scaled for the process flow rate of this study, results in approximately MM$5.104. Considering the relatively small deviations across the process units, the overall cost estimates can be deemed adequately validated for the techno-economic analysis presented.

Table 8. Estimated equipment costs for natural gas scenarios of SOFC plant.

Area	Equipment	Case 1 (MM$)	Case 2 (MM$)	Case 3 (MM$)	Case 4 (MM$)	Case 5 (MM$)
SOFC area	SOFC	27.026	27.026	27.026	27.026	27.026
	Heat Exchangers	0.039	0.040	0.092	0.045	0.024
	Compressor	2.876	2.876	2.203	2.847	2.847
	Combustor	4.654	4.806	4.654	4.079	4.079
H2S removal area	Towers	-	1.217	1.420	2.104	2.847
	Vertical Tanks	-	0.276	0.448	0.433	0.462
	Process Pump	-	0.005	0.005	0.005	0.005
CO2 removal area	Towers	-	0.215	0.423	0.538	0.569
	Vertical Tanks	-	0.164	0.229	0.290	0.343
	Compressor	-	1.976	2.103	2.212	2.307
	Process Pump	-	0.020	0.021	0.024	0.025
	Heat Exchangers	-	0.024	0.026	0.029	0.050
Steam reform area	Reformer	3.211	3.116	3.216	3.116	3.116
	Process Pump	0.011	0.011	0.011	0.011	0.011
	Heat Exchangers	0.695	0.692	0.771	0.495	0.770
Storage area	Storage Tank	2.645	2.763	2.804	2.518	2.662
Total Costs		**41.157**	**45.227**	**45.452**	**45.772**	**47.143**
		Case 6 (MM$)	Case 7 (MM$)	Case 8 (MM$)	Case 9 (MM$)	Case 10 (MM$)
SOFC area	SOFC	27.026	27.026	27.026	27.026	27.026
	Heat Exchangers	0.039	0.040	0.092	0.045	0.024
	Compressor	2.876	2.876	2.203	2.847	2.847
	Combustor	4.654	4.806	4.654	4.079	4.079
Steam reform area	Reformer	3.211	3.116	3.216	3.116	3.116
	Process Pump	0.011	0.011	0.011	0.011	0.011
	Heat Exchangers	0.695	0.692	0.771	0.495	0.770
Storage area	Storage Tank	2.645	2.387	2.203	1.527	1.247
Total Costs		**41.157**	**40.953**	**40.176**	**39.147**	**39.120**

Figure 4 illustrates the cost distribution across the evaluated scenarios. In all cases, SOFC modules represent the primary cost, accounting for around 70–80% of total plant investment—approximately MM$35. The reformer section is the second most significant contributor, representing 10–20% of costs. A noticeable trend is that increasing the biogas share in the feed leads to higher costs in pre-treatment units due to the need for larger vessels and columns. Conversely, when natural gas is predominantly used, total costs decrease. This reduction is mainly attributed to lower ethanol consumption, which in turn reduces the demand for pumps and heat exchanges related to energy integration.

The graph also correlates capital investment with LCOE. This relationship reflects not only CAPEX but also operational costs. Scenarios with higher ethanol usage exhibit elevated energy costs due to the OPEX variable costs contribution related mainly to raw material acquisition. Moreover, within the same biogas or natural gas composition, configurations with higher CAPEX also show higher LCOE values. This is explained by the extended payback time required to amortize the investment, which directly increases energy costs over the evaluated time horizon.

To estimate the Total Investment Cost (TIC), expenses are categorized into: (i) equipment costs—including spare parts, installation, and contingencies; (ii) direct field costs—piping, structural components, instrumentation, etc.; (iii) indirect field costs—civil works, services, and project management; and (iv) non-field costs—regulatory fees, logistics, contracts, and administrative expenses. After applying correction factors using APEA results and including a 10% contingency, CAPEX was estimated to range from MM$50 to MM$65 (Appendix B). Including working capital and start-up costs—covering liquidity and initial testing, the TIC varied between MM$50 and MM$70 across the ten analyzed scenarios defined previously.

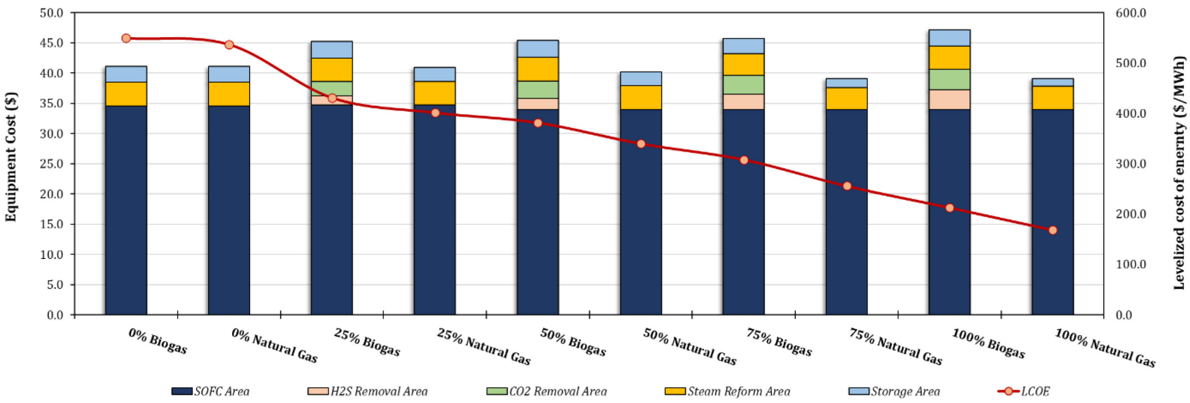

Figure 4. Equipment cost for the different scenarios and its impact on the LCOE.

Operational expenditures

To evaluate the operational expenses, it is essential to estimate the plant's variable costs, which are directly linked to the consumption of raw materials such as chemical reagents (alkalis and acids), electricity, steam, and other process utilities. These are termed variable costs because they fluctuate over time, mainly due to plant production capacity and to the volatility of commodity prices. In this study, the estimation of these costs was based on the technical coefficients detailed in Appendix C and the market prices listed in Table 6.

As illustrated in Figure 5, scenarios with lower ethanol content present significantly lower variable operational costs. This is primarily due to the high flow rate and elevated market price of ethanol, making it a major contributor to overall operating expenses. Consequently, ethanol consumption is identified as one of key factors for financial viability of the project.

Additionally, the potential revenue from the sale of solid sulphur, a byproduct of the biogas pre-treatment stage, was also accounted for. While its contribution is relatively minor, in all analyzed scenarios, the sale of this byproduct helps to partially offset external utility costs, such as processing water and base electricity consumption.

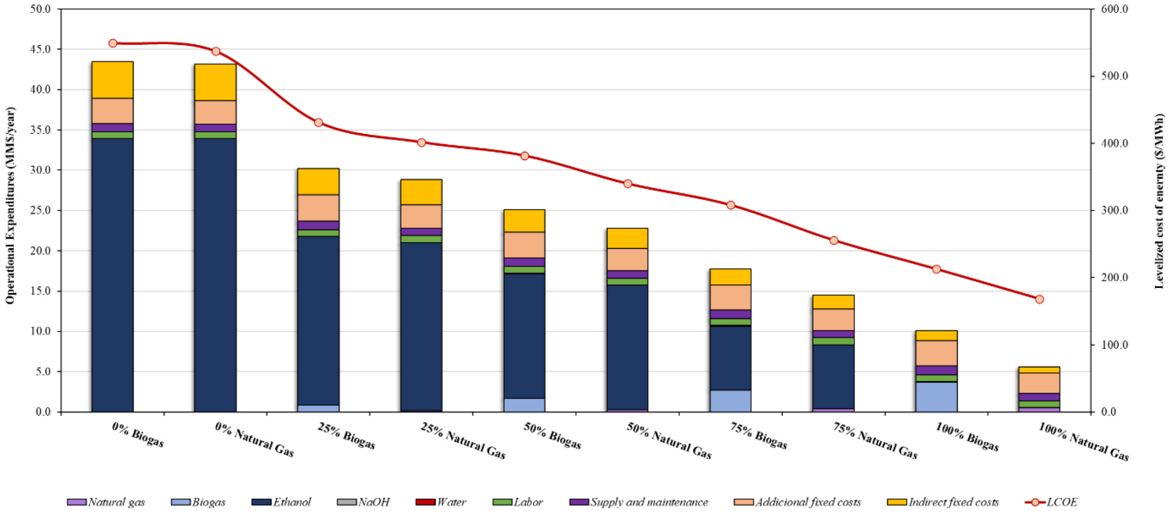

Figure 5. Operational costs breakdown for different scenarios and their corresponding impact on LCOE.

Beyond variable costs, accurate estimation of direct operating costs is also important for a comprehensive assessment of operational expenditure. These include labor (e.g., operator wages), maintenance, and related administrative charges. In contrast, indirect operating costs are associated with broader administrative and strategic functions, including management salaries, marketing, distribution, and sales. The detailed breakdown of all OPEX components is provided in Appendix A.

As expected, raw material expenses are the dominant component of OPEX (Table 9), accounting for up to 80% in the scenario utilizing 100% ethanol. The remaining 10–30% correspond mainly to indirect and auxiliary operational costs. Notably, scenarios with elevated ethanol usage exhibit the highest energy costs—up to 466 USD/MWh—substantially exceeding typical market prices for fossil-based alternatives.

Table 9. Yearly operating expenditure for SOFC-energy production.

Equipment	Case 1	Case 2	Case 3	Case 4	Case 5
Variable operating costs	3.769	10.737	17.220	21.792	33.939
Direct fixed costs	5.091	4.991	5.106	5.139	4.950
Indirect fixed costs	1.275	2.031	2.766	3.277	4.592
Total OPEX	10.137	17.760	25.093	30.209	43.482
Specific OPEX (USD/t)	99.47	174.27	246.22	296.42	426.66
	Case 6	Case 7	Case 8	Case 9	Case 10
Variable operating costs	0.545	8.362	15.726	21.032	33.939
Direct fixed costs	4.280	4.425	4.569	4.695	4.697
Indirect fixed costs	0.794	1.681	2.518	3.124	4.553
Total OPEX	5.620	14.470	22.815	28.852	43.190
Specific OPEX (USD/t)	55.15	141.99	223.87	283.11	423.79

Conversely, the most cost-effective scenarios (1 to 3 and 6 to 8), which rely on lower ethanol concentrations, achieved more competitive energy prices. A nearly linear relationship was observed between ethanol consumption and energy costs:

- A 30% reduction in ethanol usage leads to an approximate 30% reduction in energy costs.
- A 50% reduction in ethanol results in a 40–50% decrease in both operating and energy costs.

These findings underscore the strong influence of ethanol on the process's economic performance and highlight the importance of optimizing its use and exploring more cost-effective alternatives for the plant's energy matrix.

Energy Costs and Financial Comparison

To evaluate the cost of electricity produced by the SOFC unit, this study adopts the Levelized Cost of Electricity (LCOE) as the primary economic indicator. LCOE represents the average cost of generating electricity over the entire lifetime of the system, accounting for capital expenditures as well as operation and maintenance costs. It is calculated by dividing the discounted total costs by the discounted total electricity generated, providing a standardized metric for comparing different power generation technologies.

Unlike other economic approaches that incorporate revenues from byproducts or additional cash-flow components, LCOE is a purely cost-based measure. It does not include potential income from coproduct sales, carbon credits, or other financial mechanisms. This makes LCOE particularly useful for isolating the intrinsic cost of electricity generation and assessing the economic competitiveness of different feedstock and configuration scenarios.

The calculated LCOE values for all scenarios are presented in Table 10, ranging from US$ 166.93/MWh to US$ 463.39/MWh. Scenarios with lower ethanol content (Scenarios 1, 2, 6, and 7) achieve the lowest levelized costs. This trend reflects the high price of ethanol, which drives up operating expenses as its share in the fuel mixture increases.

Regarding capital investment, scenarios relying on natural gas tend to be more favorable because they do not require biogas pre-treatment units, resulting in reduced upfront costs. It is also important to note that this assessment does not include carbon capture systems or credit mechanisms; if considered, biogas-based scenarios would likely exhibit improved competitiveness. Overall, the LCOE analysis highlights how feedstock cost and system configuration directly influence the economic performance of the SOFC unit, offering a consistent and technology-agnostic basis for comparing the electricity generation cost across all scenarios.

Table 10. Yearly operating expenditure for SOFC-energy production.

Parameters	Tag name	LCOE ($/MWh)
Scenario 1	100% Biogas	166.93
Scenario 2	75% Biogas	235.32
Scenario 3	50% Biogas	302.65
Scenario 4	25% Biogas	349.63
Scenario 5	0% Biogas	466.09
Scenario 6	100% Natural Gas	112.70
Scenario 7	75% Natural Gas	194.60
Scenario 8	50% Natural Gas	273.40
Scenario 9	25% Natural Gas	330.44
Scenario 10	0% Natural Gas	463.39

Subsequently, an additional analysis was conducted to compare the electricity costs obtained with other off-grid energy sources, including hybrid diesel-photovoltaic systems, diesel-only systems, and solar systems with battery storage (Figure 6). These systems were selected because they are solutions for intermittent off-grid power generation, like SOFC technologies. This approach provides a fairer basis for comparison, as evaluating energy from an SOFC against fossil-based on-grid energy sources would not be an equitable comparison.

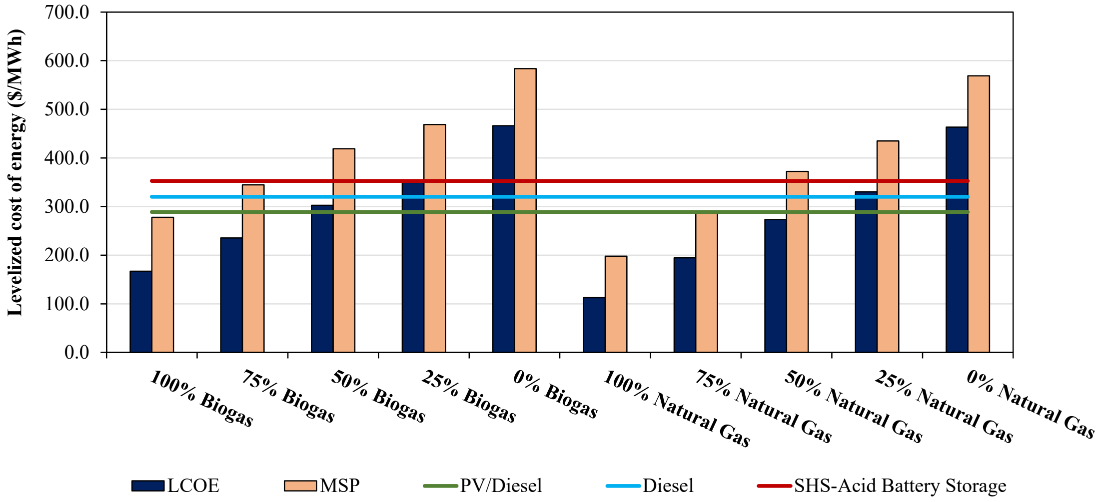

Figure 6. Energy cost comparison with other off-grid sources.

In this context, the literature indicates that the LCOE for photovoltaic cells, hybrid systems, and standalone solar systems with storage is approximately $289.00/MWh, $320.00/MWh, and $352.56/MWh, respectively [44, 45]. The analysis shows that scenarios without ethanol or with a 25% ethanol fraction in the process exhibit energy costs lower than those reported in the literature. This highlights the competitive potential of these scenarios within the current off-grid energy landscape. The results are promising and suggest that SOFC technology is a viable alternative to existing off-grid solutions.

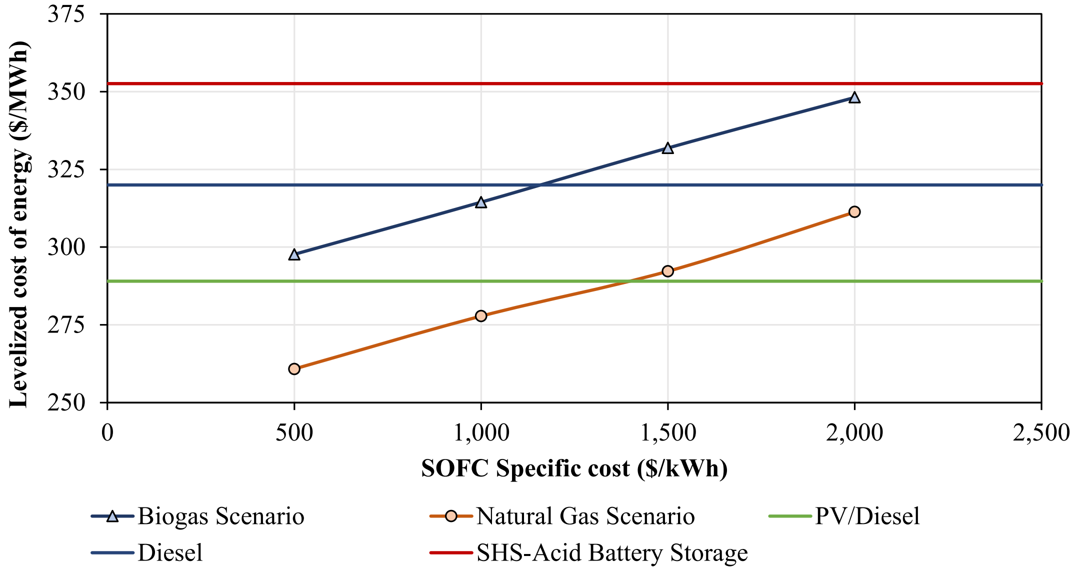

Figure 7. Energy cost with different SOFC specific costs compared with other off-grid sources.

Additionally, a second analysis was performed by varying the specific cost of SOFC technology, as shown in Figure 7. In this case, only the baseline scenario with 50% ethanol content was evaluated. The specific cost variation ranged from $500/kWh to $2,000/kWh. All scenarios remained below the electricity price of solar panels, with natural gas-based configurations proving more competitive than diesel-based ones. This result is also encouraging, as it underscores the importance of SOFC technology costs in determining the feasibility of the process. The insights from these two analyses also shed light on both operational costs—particularly ethanol consumption—and the capital cost of SOFC technology.

Sensitivity Analysis

The technology studied is subject to a series of uncertainties and is highly dependent on factors such as production capacity, feedstock costs (particularly ethanol), capital investment, and others. To assess the sensitivity of these variables, a tornado analysis (Figure 8) was conducted by applying positive and negative fluctuations to key parameters to evaluate their impact on project feasibility and financial performance indicators.

A set of key variables was selected for this analysis, including CAPEX, ethanol cost, biogas cost, production capacity, rate of return, taxes, and electricity selling price. The applied fluctuations ranged from ±25% for certain variables to ±15% for others. The base scenario (50% ethanol – 50% biogas) was chosen as the reference case, with its financial indicators as the baseline for comparison.

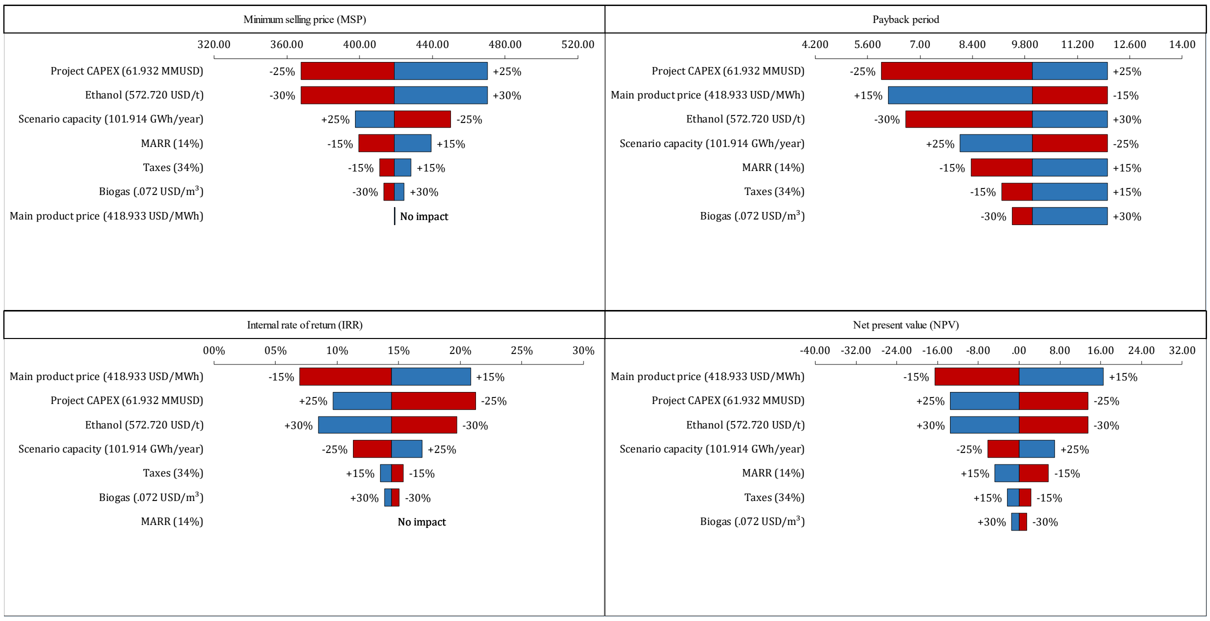

Figure 8. Tornado chart of different impacts on financial key parameters.

The main financial responses analysed included the electricity selling price, payback time, internal rate of return (IRR), and net present value (NPV). Across scenarios, a consistent pattern emerged, where the electricity price, CAPEX, and ethanol cost were the variables with the most significant influence on financial outcomes. Regarding payback time, a 25% increase in costs can render the project unfeasible within the investment horizon. Conversely, a 25% decrease in CAPEX can reduce the payback period by approximately four years. For the internal rate of return, the electricity selling price was the most impactful variable—a predictable result given its direct relationship with project revenue. Even small increases in the electricity price significantly improve the IRR. In terms of MSP of electricity, CAPEX proved to be the most influential factor, followed by ethanol price and process capacity. This reinforces earlier findings: the technology's cost plays a major role in economic viability. Ethanol's high price and consumption rate substantially increase operating costs. Additionally, scaling up the system demonstrates movement along the cost curve, suggesting that the current plant size has not yet reached an asymptotic cost minimum. Therefore, there is clear potential for capacity expansion to further reduce the final cost of electricity.

Finally, since CAPEX and ethanol cost were identified as the most influential variables throughout the analysis, an additional study was carried out to investigate their specific effects on the LCOE. In this assessment, the specific cost of the SOFC system was varied between $500/MWh to $5000/MWh, while the ethanol purchase price ranged from $272.72/t to $872.72/t (Figure 9).

As expected, higher ethanol prices and higher SOFC technology costs result in increased LCOE, while reductions in these costs lead to lower LCOE values. However, a deeper analysis reveals an important asymmetry: a 25% increase in ethanol price leads to approximately a 10% rise in LCOE, whereas a 25% increase in the specific SOFC capital cost results in only a 2% increase in LCOE. This clearly indicates that operating costs, particularly ethanol, have a much stronger impact on project viability compared to capital expenditures. When the ethanol price is doubled (a 50% increase), the LCOE can rise by around 50%, while doubling the specific capital cost leads to only an 8% increase in LCOE. These findings highlight the nonlinear and non-parallel sensitivities of each variable on the system's cost structure.

The heat map produced from this analysis further illustrates that, for every 10% increase in ethanol cost, a corresponding 2% reduction in SOFC technology cost would be required to maintain competitiveness. This is especially relevant when benchmarking against other intermittent renewable technologies such as photovoltaic systems with battery storage, which currently achieve LCOE values around $352.56/MWh. Therefore, optimizing ethanol procurement strategies and exploring more affordable feedstock options may be more impactful for improving the system's economic performance than solely reducing capital costs.

Output variable		Ethanol price ($/t)												
LCOE ($/MWh)		272.72	322.72	372.72	422.72	472.72	522.72	572.72	622.72	672.72	722.72	772.72	822.72	872.72
SOFC Specific CAPEX ($/kWh)	500.00	235.63	248.88	262.13	275.38	288.63	301.88	315.14	328.39	341.64	354.89	368.14	381.39	394.64
	750.00	243.03	256.28	269.53	282.78	296.03	309.28	322.54	335.79	349.04	362.29	375.54	388.79	402.04
	1,000.00	250.43	263.68	276.93	290.18	303.43	316.68	329.93	343.19	356.44	369.69	382.94	396.19	409.44
	1,250.00	257.83	271.08	284.33	297.58	310.83	324.08	337.33	350.58	363.84	377.09	390.34	403.59	416.84
	1,500.00	265.23	278.48	291.73	304.98	318.23	331.48	344.73	357.98	371.23	384.49	397.74	410.99	424.24
	1,750.00	272.63	285.88	299.13	312.38	325.63	338.88	352.13	365.38	378.63	391.89	405.14	418.39	431.64
	2,000.00	280.03	293.28	306.53	319.78	333.03	346.28	359.53	372.78	386.03	399.28	412.54	425.79	439.04
	2,500.00	294.83	308.08	321.33	334.58	347.83	361.08	374.33	387.58	400.83	414.08	427.33	440.59	453.84
	3,000.00	309.62	322.87	336.13	349.38	362.63	375.88	389.13	402.38	415.63	428.88	442.13	455.38	468.63
	3,500.00	324.42	337.67	350.92	364.18	377.43	390.68	403.93	417.18	430.43	443.68	456.93	470.18	483.43
	4,000.00	339.22	352.47	365.72	378.97	392.22	405.48	418.73	431.98	445.23	458.48	471.73	484.98	498.23
	4,500.00	354.02	367.27	380.52	393.77	407.02	420.27	433.53	446.78	460.03	473.28	486.53	499.78	513.03
	5,000.00	368.82	382.07	395.32	408.57	421.82	435.07	448.32	461.58	474.83	488.08	501.33	514.58	527.83

Figure 9. Sensitivity surface of the effect of SOFC-specific technology cost and ethanol price on the LCOE.

CONCLUSIONS

The model developed for SOFC technology enabled a robust analysis of the cell behavior under variations in temperature and current density. This model was entirely based on literature-reported parameters and equations under steady-state conditions. It exhibited a strong fit with expected performance, particularly in terms of power output and polarization losses.

Regarding cost estimation, capital expenditure for equipment acquisition ranged from MM$39 to MM$47, with total investment reaching between MM$50 and MM$70. In all scenarios, SOFC modules were the main cost drivers, representing approximately 70–80% of the total investment—around $35 million—consistent with values found in the literature. Operational costs revealed ethanol procurement as the most significant contributor in scenarios that involve its use. Overall, scenarios 1, 2, 3, 6, 7, and 8 demonstrated higher economic viability, primarily due to lower ethanol usage. Among them, scenarios 6, 7, and 8 stood out further, as they utilize natural gas from the grid, eliminating the need for biogas pre-treatment units and reducing associated costs.

The comparative analysis showed that SOFC technology has the potential to achieve lower LCOE values than well-established technologies such as batteries, photovoltaic systems, and diesel generators. This project sheds light on key technological and economic challenges, reinforcing that as the technology matures and gains scale, acquisition and implementation costs are expected to decline—making SOFC-based energy solutions increasingly competitive in the future.

ACKNOWLEDGMENTS

The authors gratefully acknowledge Repsol Sinopec Brasil for its financial and technical support and ANP (Brazilian National Oil, Natural Gas, and Biofuels Agency) for the strategic importance of its support through the R&D levy regulation.

NOMENCLATURE

Symbols

A	cell area	[m²]
A_K	empirical factor	[Ω·m]
B_K	empirical factor	[Ω·m]
D_{eff,H_2}	effective diffusivity of hydrogen	[m²/s]
$D_{i,j}$	binary diffusivity	[m²/s]
$D_{i,k}$	Knudsen diffusivity	[m²/s]
E^0	standard cell potential at reference temperature	[J/mol]
E	activation energy	[J/mol]
F	Faraday constant	[C/mol]
i	current density	[A/m²]
i_0	exchange current density	[A/m²]
i_L	limiting current density	[A/m²]
M	molar mass of species	[kg/mol]
n_e	number of electrons	[—]
$n_{H_{2,cons}}$	molar flow rate of hydrogen consumed	[kmol/h]
$n_{H_{2,in}}$	molar flow rate of hydrogen in the feed	[kmol/h]
N	number of cells	[—]
P	system pressure	[bar]
R	universal gas constant	[J/mol·K]
r_k	resistance	[Ω]
r_{por}	pore radius	[m]
T_{SOFC}	SOFC temperature	[K]
U_f	fuel utilization factor	[—]
V	voltage	[V]
W	cell power	[W]

Greek letters

β	empirical factor	[—]
ε	electrode porosity	[—]
γ	pre-exponential factor	[A/m²]
ρ	specific resistivity	[Ω.m]
τ	tortuosity factor	[—]
σ	collision diameter	[m²]
δ	material thickness	[m]

Subscripts and superscripts

act	activation
an	anode
ca	cathode
Cell	cell

conc	concentration
Eff	effective
L	limiting
Nerst	nerst
Ohm	ohmic
por	Pore

Abbreviations

APEA	Aspen Process Economic Analysis
CAPEX	Capital Expenditure
ED	Ethanol Decomposition
EH	Ethanol Dehydrogenation
ESR	Ethanol Steam Reforming
IRR	Internal Rate of Return
LCOE	Levelized Cost of Electricity
LHHW	Langmuir-Hinshelwood-Hougen-Watson
MARR	Minimum Acceptance Rate of Return
MSP	Minimum Selling Price
NPV	Net Present Value
OPEX	Operational Expenditure
SMR	Steam Methane Reforming
SOFC	Solid Oxide Fuel Cells
SR	Steam Reforming
TIC	Total Investment Costs
WGSR	Water-Gas Shift Reaction

REFERENCES

1. D. J. Tashevski and D. M. Dimitrovski, “Optimization of binary co-generative thermal power plants with SOFC on solid fuel,” Chemical Engineering Transactions, vol. 34, pp. 31–36, 2013.
2. M. Lamagna, B. Nastasi, D. Groppi, C. Rozain, M. Manfren, and D. A. Garcia, “Techno-economic assessment of reversible solid oxide cell integration to renewable energy systems at building and district scale,” Energy Conversion and Management, vol. 235, 113993, 2021.
3. H. Guo, W. Gu, M. Khayatnezhad, and N. Ghadimi, “Parameter extraction of the SOFC mathematical model based on fractional order version of dragonfly algorithm,” International Journal of Hydrogen Energy, vol. 47, no. 57, pp. 24059–24068, 2022.
4. A. V. Akkaya, “Electrochemical model for performance analysis of a tubular SOFC,” International Journal of Energy Research, vol. 31, no. 1, pp. 79–98, 2007.
5. S. H. Chan, K. A. Khor, and Z. T. Xia, “A complete polarization model of a solid oxide fuel cell and its sensitivity to the change of cell component thickness,” Journal of Power Sources, vol. 93, no. 1–2, pp. 130–140, 2001.
6. S. H. Chan, C. F. Low, and O. L. Ding, “Energy and exergy analysis of simple solid-oxide fuel-cell power systems,” Journal of Power Sources, vol. 103, no. 2, pp. 188–200, 2002.
7. T. A. De Souza, C. J. Coronado, J. L. Silveira, and G. M. Pinto, “Economic assessment of hydrogen and electricity cogeneration through steam reforming–SOFC system in the Brazilian biodiesel industry,” Journal of Cleaner Production, vol. 279, 123814, 2021.
8. P. Tippawan and A. Arpornwichanop, “Energy and exergy analysis of an ethanol reforming process for solid oxide fuel cell applications,” Bioresource Technology, vol. 157, pp. 231–239, 2014.

9. M. Gustafsson et al., “A perspective on the state of the biogas industry from selected member countries,” IEA Bioenergy Task, vol. 37, no. 2024, p. 2, 2024.
10. R. Turton, R. C. Bailie, W. B. Whiting, and J. A. Shaeiwitz, Analysis, Synthesis and Design of Chemical Processes, Pearson Education, 2008.
11. M. F. Abdel Hamid, T. M. Aboul-Fotouh, and M. A. El-Shafie, “A comparison between Claus and THIOPAQ sulfur recovery techniques in natural gas plants,” Journal of Engineering and Applied Science, vol. 71, no. 1, p. 27, 2024.
12. W. Wan, “An innovative system by integrating the gasification unit with the supercritical water unit to produce clean syngas for solid oxide fuel cell (SOFC): System performance assessment,” International Journal of Hydrogen Energy, vol. 41, no. 48, pp. 22698–22710, 2016.
13. J. I. Huertas, N. Giraldo, and S. Izquierdo, “Removal of H_2S and CO_2 from biogas by amine absorption,” in Mass Transfer in Chemical Engineering Processes, pp. 307–333, 2011.
14. Agência Nacional do Petróleo, Gás Natural e Biocombustíveis (ANP), Resolução ANP No. 906, de 18 de Novembro de 2022 — Specifications of biomethane derived from organic agro-silvopastoral and commercial residues for vehicular, residential and commercial use (in Portuguese), Diário Oficial da União, no. 221, 24 Nov. 2022. Available online: atosoficiais.com.br/anp/resolucao-n-906-2022…, [Accessed: 29-Oct-2024].
15. J. Heo, B. Lee, S. Kim, J. N. Kim, and H. Lim, “Techno-economic analysis of a biological desulfurization process for a landfill gas in Korea,” Separation Science and Technology, vol. 53, no. 17, pp. 2769–2781, 2018.
16. L. C. Moreira, P. O. Borges, R. M. Cavalcante, and A. F. Young, “Simulation and economic evaluation of process alternatives for biogas production and purification from sugarcane vinasse,” Renewable and Sustainable Energy Reviews, vol. 163, 112532, 2022.
17. P. Cozma, W. Wukovits, I. Mămăligă, A. Friedl, and M. Gavrilescu, “Modeling and simulation of high pressure water scrubbing technology applied for biogas upgrading,” Clean Technologies and Environmental Policy, vol. 17, pp. 373–390, 2015.
18. E. Ryckebosch, M. Drouillon, and H. Vervaeren, “Techniques for transformation of biogas to biomethane,” Biomass and Bioenergy, vol. 35, no. 5, pp. 1633–1645, 2011.
19. D. W. Allen, E. R. Gerhard, and M. R. Likins Jr., “Kinetics of the methane–steam reaction,” Industrial & Engineering Chemistry Process Design and Development, vol. 14, no. 3, pp. 256–259, 1975.
20. A. N. Fatsikostas and X. E. Verykios, “Reaction network of steam reforming of ethanol over Ni-based catalysts,” Journal of Catalysis, vol. 225, no. 2, pp. 439–452, 2004.
21. J. Zhou, Z. Wang, M. Han, Z. Sun, and K. Sun, “Optimization of a 30 kW SOFC combined heat and power system with different cycles and hydrocarbon fuels,” International Journal of Hydrogen Energy, vol. 47, no. 6, pp. 4109–4119, 2022.
22. I. Uriz, G. Arzamendi, E. Lopez, J. Llorca, and L. M. Gandía, “Computational fluid dynamics simulation of ethanol steam reforming in catalytic wall microchannels,” Chemical Engineering Journal, vol. 167, no. 2–3, pp. 603–609, 2011.
23. P. Iora, P. Aguiar, C. S. Adjiman, and N. P. Brandon, “Comparison of two IT DIR–SOFC models: Impact of variable thermodynamic, physical, and flow properties. Steady-state and dynamic analysis,” Chemical Engineering Science, vol. 60, no. 11, pp. 2963–2971, 2005.
24. S. A. Hajimolana, M. A. Hussain, W. A. W. Daud, M. Soroush, and A. Shamiri, “Mathematical modeling of solid oxide fuel cells: A review,” Renewable and Sustainable Energy Reviews, vol. 15, no. 4, pp. 1893–1917, 2011.
25. H. Ghezel-Ayagh, Solid oxide electrolysis system demonstration, FuelCell Energy Inc. / US DOE, 2021.

26. M. Hauck, S. Herrmann, and H. Spliethoff, “Simulation of a reversible SOFC with Aspen Plus,” International Journal of Hydrogen Energy, vol. 42, no. 15, pp. 10329–10340, 2017.
27. D. Saebea, A. Arpornwichanop, and Y. Patcharavorachot, “Thermodynamic analysis of a proton conducting SOFC integrated system fuelled by different renewable fuels,” International Journal of Hydrogen Energy, vol. 46, no. 20, pp. 11445–11457, 2021.
28. W. Zhang, E. Croiset, P. L. Douglas, M. W. Fowler, and E. Entchev, “Simulation of a tubular solid oxide fuel cell stack using AspenPlus™ unit operation models,” Energy Conversion and Management, vol. 46, no. 2, pp. 181–196, 2005.
29. G. Yanalak et al., “Photocatalytic hydrogen evolution reaction activity comparable to 1-D nanofiber materials exhibited by the kesterite nanorods catalysts,” Renewable Energy, pp. 469–475, 2020.
30. S. Jankhah, N. Abatzoglou, and F. Gitzhofer, “Thermal and catalytic dry reforming and cracking of ethanol for hydrogen and carbon nanofilaments’ production,” International Journal of Hydrogen Energy, vol. 33, no. 9, pp. 4769–4779, 2008.
31. W. Chen et al., “Design and optimization of a crossflow tube reactor system for hydrogen production by combining ethanol steam reforming and water–gas shift reaction,” Fuel, vol. 341, 126628, 2023.
32. J. Xu and G. F. Froment, “Methane steam reforming, methanation and water–gas shift: I. Intrinsic kinetics,” AIChE Journal, vol. 35, no. 1, pp. 88–96, 1989.
33. M. Rahimpour, Z. Arab Aboosadi, and A. Jahanmiri, “Synthesis gas production in a novel hydrogen and oxygen perm-selective membrane tri-reformer for methanol production,” Journal of Natural Gas Science and Engineering, vol. 10, pp. 149–159, 2012.
34. J. Welty, G. L. Rorrer, and D. G. Foster, Fundamentals of Momentum, Heat, and Mass Transfer, John Wiley & Sons, 2014.
35. Statistics Finland, Official Statistics of Finland (OSF): Population structure. Helsinki, 2016.
36. I. J. Okeke and S. Mani, “Techno-economic assessment of biogas to liquid fuels conversion technology via Fischer–Tropsch synthesis,” Biofuels, Bioproducts and Biorefining, vol. 11, no. 3, pp. 472–487, 2017.
37. European Biogas Association, Biogas cost reductions to boost sustainable transport, IRENA, 2024.
38. Intratec Solutions, Utility Cost Database, 2025.
39. A. L. Facci, V. Cigolotti, E. Jannelli, and S. Ubertini, “Technical and economic assessment of a SOFC-based energy system for combined cooling, heating and power,” Applied Energy, vol. 192, pp. 563–574, 2017.
40. G. Diglio et al., “Techno-economic analysis of sorption-enhanced steam methane reforming in a fixed bed reactor network integrated with fuel cell,” Journal of Power Sources, vol. 364, pp. 41–50, 2017.
41. L. B. Allegue and J. Hinge, Biogas upgrading: Evaluation of methods for H_2S removal, Danish Technological Institute, 2014.
42. F. Bauer, C. Hulteberg, T. Persson, and D. Tamm, Biogas upgrading — review of commercial technologies, Swedish Gas Technology Centre (SGC), 2013.
43. F. Magli, F. Capra, M. Gatti, and E. Martelli, “Process selection, modelling and optimization of a water scrubbing process for energy-self-sufficient biogas upgrading plants,” Sustainable Energy Technologies and Assessments, vol. 27, pp. 63–72, 2018.
44. D. Tsuanyo, Y. Azoumah, D. Aussel, and P. Neveu, “Modeling and optimization of batteryless hybrid PV/diesel systems for off-grid applications,” Energy, vol. 86, pp. 152–162, 2015.
45. S. P. Ayeng'o, T. Schirmer, K. P. Kairies, H. Axelsen, and D. U. Sauer, “Comparison of off-grid power supply systems using lead-acid and lithium-ion batteries,” Solar Energy, vol. 162, pp. 140–152, 2018.

APPENDIX

Operational expenditures typical ranges

Table A.1: Operational expenditures typical ranges and chosen values for the analysis.

Fator	Typical ranges	Chosen values
Raw material	CRW	CRW
Utilities	CUT	CUT
Variable costs (VC)	CRW + CUT	
Operations team	COT	COT
Laboratories expenses	(0,1-0,2) COT	0,1 COT
Office labor	(0,1-0,25) COT	0,1 COT
Operating supplies	(0,1-0,2) (0,06 CAPEX)	0,002 CAPEX
Maintenance and repairs	(0,02-0,1) CAPEX	0,01 CAPEX
Administrative overhead	(0,5-0,7) 1,18 COT	0,55 COT
Manufacturing overhead	(0,5-0,7) 0,06 CAPEX	0,007 CAPEX
Fees and insurance	(0,014-0,05) CAPEX	0,05 CAPEX
Patents e royalties	(0,00-0,06) OPEX	0,01 OPEX
Direct fixed costs (DFC)	0,75 COT + 0,069 CAPEX + 0,01 OPEX	
Administrative costs	(0,165-0,1875) COT	0,165 COT
General costs	0,0015 CAPEX	0,0015 CAPEX
Distribution and sales	(0,02-0,2) OPEX	0,08 OPEX
Research and development	0,05 OPEX	0,02 OPEX
Indirect fixed costs (IFC)	0,165 COT + 0,002 CAPEX + 0,1 OPEX	
Total operating costs (OPEX)	0,079 CAPEX + 2,152 COT + 1,124 VC	

Investment cost breakdown

Table A.2. Total investment cost breakdown.

Item	Case 1 (MM$)	Case 2 (MM$)	Case 3 (MM$)	Case 4 (MM$)	Case 5 (MM$)
Equipment acquisition, spare parts, equipment settings and unscheduled equipment					
Total equipment costs	51.268	49.783	49.428	49.184	44.760
Piping, civil, steel, instrumentals, electrical, insulation, paint					
Total direct field costs	4.621	4.529	4.454	4.432	4.039
Field office staff and construction indirect					
Total indirect field costs	1.882	1.834	1.814	1.805	1.645
Freight, taxes, and permits, engineering, general expenses, contract fees					
Total non-field costs	4.803	3.482	4.629	4.606	4.198
ISBL + OSBL total costs	62.574	59.629	60.326	60.027	54.641
Contingency			10%		
Time update factor			0.96		
Location factor			0.97		
CAPEX	64.240	61.217	61.932	61.625	56.096
Specific CAPEX (USD/MWh)	630.34	600.67	607.69	604.68	550.43
Working capital	1.285	1.224	1.239	1.233	1.122
Start-up costs	1.285	1.224	1.239	1.233	1.122
Total Investment Cost (TIC)	66.810	63.666	64.409	64.090	58.340
Specific TIC (USD/MWh)	655.55	624.70	632.00	628.87	572.45
Item	**Case 6 (MM$)**	**Case 7 (MM$)**	**Case 8 (MM$)**	**Case 9 (MM$)**	**Case 10 (MM$)**
Equipment acquisition, spare parts, equipment settings and unscheduled equipment					
Total equipment costs	41.425	42.400	43.475	44.329	44.194
Piping, civil, steel, instrumentals, electrical, insulation, paint					
Total direct field costs	3.407	3.388	3.375	3.472	2.562
Field office staff and construction indirect					
Total indirect field costs	1.387	1.410	1.374	1.413	1.043
Freight, taxes, and permits, engineering, general expenses, contract fees					
Total non-field costs	3.541	3.521	3.507	3.608	2.663
ISBL + OSBL total costs	49.759	50.719	51.731	52.822	50.462
Contingency			10%		
Time update factor			0.96		
Location factor			0.97		
CAPEX	51.084	52.070	53.109	54.228	51.806
Specific CAPEX (USD/MWh)	521.12	510.92	521.12	532.10	508.33
Working capital	1.062	1.041	1.062	1.085	1.036
Start-up costs	1.062	1.041	1.062	1.085	1.036
Total Investment Cost (TIC)	55.233	54.153	55.233	56.397	53.878
Specific TIC (USD/MWh)	541.96	531.36	541.96	553.38	528.66

Technical Coefficients

Table A.3. Technical coefficient of the evaluated scenarios.

Item	Unit	Case 1	Case 2	Case 3	Case 4	Case 5
Main Product						
Energy power	MW/MW	1.000	1.000	1.000	1.000	1.000
Biogas - H_2S removal section						
Biogas feed	[kg/kg of H_2S-free biogas]	1.010	1.010	1.025	1.011	-
NaOH	[kg/kg of H_2S-free biogas]	0.001	0.001	0.001	0.001	-
Sulfur	[kg/kg of H_2S-free biogas]	0.002	0.002	0.002	0.002	-
H_2S-free biogas	[kg/kg of H_2S-free biogas]	1.000	1.000	1.000	1.000	-
Biogas - CO_2 removal section						
H_2S-free biogas	[kg/kg of CO_2-free biogas]	3.294	3.294	3.221	3.288	-
Water	[kg/kg of CO_2-free biogas]	5.361	5.360	5.269	5.349	-
Steam	[kg/kg of CO_2-free biogas]	6.678	6.679	6.625	6.671	-
CO_2-free biogas	[kg/kg of CO_2-free biogas]	1.000	1.000	1.000	1.000	-
Steam reforming						
CO_2-free biogas	[kg/kg of H_2]	2.824	2.079	1.320	0.666	0.000
Ethanol	[kg/kg of H_2]	-	2.152	4.181	5.649	7.386
Water	[kg/kg of H_2]	8.333	5.957	5.163	4.824	4.343
H_2	[kg/kg of H_2]	1.000	1.000	1.000	1.000	1.000
SOFC						
H_2	[kg/MW]	59.75	59.75	59.75	59.75	59.75
Air	[kg/MW]	3,096	3,096	3,096	3,096	3,096
Power	[MW/MW]	1.000	1.000	1.000	1.000	1.000
Item	**Unit**	**Case 6**	**Case 7**	**Case 8**	**Case 9**	**Case 10**
Main Product						
Energy power	MW/MW	1.000	1.000	1.000	1.000	1.000
Steam reforming						
CO_2-free biogas	[kg/kg of H_2]	2.824	2.079	1.320	0.666	0.000
Ethanol	[kg/kg of H_2]	-	2.152	4.181	5.649	7.386
Water	[kg/kg of H_2]	8.333	5.957	5.163	4.824	4.343
H_2	[kg/kg of H_2]	1.000	1.000	1.000	1.000	1.000
SOFC						
H_2	[kg/MW]	59.75	59.75	59.75	59.75	59.75
Air	[kg/MW]	3,096	3,096	3,096	3,096	3,096
Power	[MW/MW]	1.000	1.000	1.000	1.000	1.000